

Van der Waals isotope heterostructures for engineering phonon polariton dispersions

Received: 8 February 2023

Accepted: 26 July 2023

Published online: 08 August 2023

 Check for updatesM. Chen^{1,8}, Y. Zhong^{2,8}, E. Harris³, J. Li⁴, Z. Zheng⁵, H. Chen^{2,6}, J.-S. Wu⁷, P. Jarillo-Herrero⁵, Q. Ma³, J. H. Edgar⁴, X. Lin² & S. Dai¹ ✉

Element isotopes are characterized by distinct atomic masses and nuclear spins, which can significantly influence material properties. Notably, however, isotopes in natural materials are homogeneously distributed in space. Here, we propose a method to configure material properties by repositioning isotopes in engineered van der Waals (vdW) isotopic heterostructures. We showcase the properties of hexagonal boron nitride (hBN) isotopic heterostructures in engineering confined photon-lattice waves—hyperbolic phonon polaritons. By varying the composition, stacking order, and thicknesses of $h^{10}\text{BN}$ and $h^{11}\text{BN}$ building blocks, hyperbolic phonon polaritons can be engineered into a variety of energy-momentum dispersions. These confined and tailored polaritons are promising for various nanophotonic and thermal functionalities. Due to the universality and importance of isotopes, our vdW isotope heterostructuring method can be applied to engineer the properties of a broad range of materials.

Element isotopes exist universally and distribute evenly in space (Fig. 1a). Various isotopes have the same number of protons (and electrons) but differ in the numbers of neutrons in the nuclei. Therefore, they possess distinct atomic masses and nuclear spins. The variation in atomic mass affects the nuclear structures^{1,2}, rate of chemical reactions³, and lattice vibrations^{4–6} that govern thermal^{7–10} and elastic responses¹¹. Electronic properties¹², including superconductivity¹³, transport¹⁴, excitons^{10,15}, and band structures, also vary with isotopes via electron-phonon interactions. In addition, isotopes offer an important resource for quantum technologies^{16–20} by altering the nuclear spin-related properties for quantum preservation and qubit encoding. These isotope-related merits were facilitated by isotope purifications that globally alter the overall isotope ratios in materials^{1–20}. Notably, both naturally abundant and isotopically purified crystals are isotope-homogeneous: all isotopes distribute evenly in space.

In this work, we explore the isotope spatial-heterogeneity by establishing a materials engineering method called van der Waals (vdW) isotope heterostructuring. vdW isotope heterostructuring configures material properties by repositioning isotopes in engineered isotopic heterostructures (Fig. 1b). The advance of this method lies in that fundamental material parameters—atomic mass and nuclear spin—of the same element can vary internally in materials and be spatially engineered. Therefore, intrinsic material responses can be reshaped from an internal perspective to offer virtues absent in current isotope-homogeneous systems. We showcase vdW isotope heterostructuring in engineering confined photon-lattice waves—hyperbolic phonon polaritons (HPPs)^{21–30}—in hexagonal boron nitride (hBN) isotopic heterostructures. By varying the composition, stacking, and thicknesses of monoisotopic ^{10}B and ^{11}B vdW building blocks, HPPs can be engineered into a variety of energy (ω)-momentum (k) dispersions that break the universal even-dispersion in hyperbolic materials^{31–40}. These

¹Materials Research and Education Center, Department of Mechanical Engineering, Auburn University, Auburn, AL 36849, USA. ²Interdisciplinary Center for Quantum Information, State Key Laboratory of Modern Optical Instrumentation, ZJU-Hangzhou Global Science and Technology Innovation Center, Zhejiang University, Hangzhou 310027, China. ³Department of Physics, Boston College, Chestnut Hill, Massachusetts, MA 02467, USA. ⁴Tim Taylor Department of Chemical Engineering, Kansas State University, Manhattan, KS 66506, USA. ⁵Department of Physics, Massachusetts Institute of Technology, Cambridge, Massachusetts, MA 02139, USA. ⁶International Joint Innovation Center, The Electromagnetics Academy at Zhejiang University, Zhejiang University, Haining 314400, China. ⁷Department of Photonics and Institute of Electro-Optical Engineering, National Yang Ming Chiao Tung University, Hsinchu 30050, Taiwan. ⁸These authors contributed equally: M. Chen, Y. Zhong. ✉ e-mail: sdai@auburn.edu

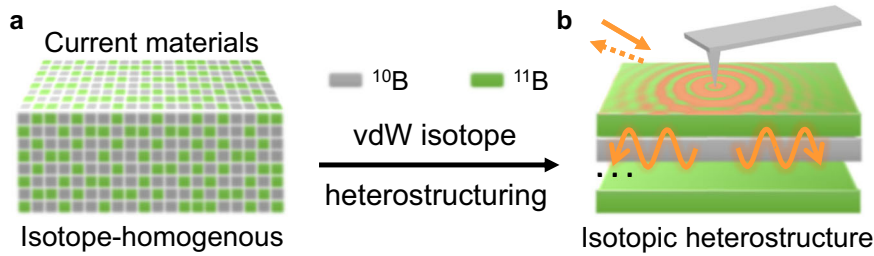


Fig. 1 | The schematic of van der Waals isotope heterostructuring showcased in phonon polaritons in hBN isotopic heterostructures. a current materials are isotope-homogenous: isotopes always distribute evenly in space. **b** experiment

schematic of s-SNOM imaging of engineered hyperbolic phonon polaritons in ^{10}B - ^{11}B isotopic heterostructures.

confined and tailored polaritons may offer on-demand nano-light for various nanophotonic and thermal functionalities. The method of vdW isotope heterostructuring showcased here can also apply to a broad range of materials and properties due to the universality and importance of isotopes.

Results

Imaging of phonon polaritons in isotopic heterostructures

Engineered HPPs in isotopic heterostructures were characterized by infrared nano-imaging using scattering-type scanning near-field optical microscopy (s-SNOM, method). The s-SNOM is an illuminated atomic force microscope (AFM) that simultaneously delivers topography and nano-optical image of the underneath sample (Fig. 1b). In the experiment, the AFM tip acts as an antenna⁴¹ to bridge the momentum mismatch and transfer energy between free-space infrared (IR) light (wavelength λ_0 and frequency $\omega = 1/\lambda_0$) and HPPs^{42,43}. The s-SNOM observable near-field amplitude $S(\omega)$ possesses a spatial resolution of ~ 10 nm. Therefore, it can map HPPs and other nano-optical phenomena in real space.

The crystalline anisotropy of hBN leads to natural hyperbolicity ($\epsilon_x\epsilon_z < 0$, $\epsilon_x = \epsilon_y = \epsilon_z$ and ϵ_z are in-plane and vertical permittivity, respectively) and HPPs inside the Reststrahlen bands^{21,25}. HPPs are typically imaged by s-SNOM as parallel fringes^{21–25}—standing wave interference between tip-launched and edge-reflected HPPs (Fig. 1b). The fringe period is proportional to the HPP wavelength λ_p . In the s-SNOM images (Fig. 2), fringes show the strongest oscillation closest to crystal edges, followed by weakly damped ones away from the edges. These characteristics are revealed evidently in s-SNOM profiles (gray and green curves in Fig. 2c, d)—line cuts of the s-SNOM images (gray and blue dashed lines in Fig. 2a, b)—of the ^{10}B and ^{11}B hBN. HPPs in ^{10}B and ^{11}B hBN exhibit different energy (ω)-momentum ($k = 2\pi/\lambda_p$) dispersions: they show different λ_p at $\omega = 1440$ cm^{-1} and 1420 cm^{-1} (Fig. 2a, b) and HPPs at $\omega = 1380$ cm^{-1} and 1385 cm^{-1} can only be imaged in ^{11}B hBN (Fig. 2c, d). This dispersion variation originates from the different atomic masses that yield Reststrahlen band $\omega = 1394.5$ cm^{-1} to 1650 cm^{-1} and 1359.8 cm^{-1} to 1608.7 cm^{-1} , for ^{10}B and ^{11}B hBN, respectively⁴⁴.

The dispersion variation between ^{10}B and ^{11}B hBN facilitates the engineering of HPPs in their stacked hybrids—*isotopic heterostructures*. At representative IR frequencies (Fig. 2), HPPs were imaged in ^{10}B - ^{11}B isotopic heterostructures with distinctive characteristics. Close to the edges of isotopic heterostructures (e.g., Fig. 2a, b), HPPs exhibit short-period beats in addition to long-period fringes. As detailed in the s-SNOM profiles (Fig. 2c, d), the short-period beats in ^{10}B - ^{11}B isotopic heterostructures (black, red, blue, cyan, and pink curves) show narrower oscillation features than the fringes in single slab ^{10}B and ^{11}B hBN (gray and green curves). These beats typically do not appear in s-SNOM images of hBN^{21–24}. Moreover, HPPs in isotopic heterostructures depend strongly on the composition and stacking of the ^{10}B and ^{11}B building blocks. HPPs in the 2-slab heterostructure with stacking (from top to bottom) $^{10}\text{B}|^{10}\text{B}$, $^{10}\text{B}|^{11}\text{B}$, $^{11}\text{B}|^{10}\text{B}$, $^{11}\text{B}|^{11}\text{B}$, 3-slab

heterostructure $^{10}\text{B}|^{11}\text{B}|^{11}\text{B}$, $^{11}\text{B}|^{10}\text{B}|^{11}\text{B}$, $^{11}\text{B}|^{11}\text{B}|^{10}\text{B}$, $^{10}\text{B}|^{10}\text{B}|^{11}\text{B}$, $^{10}\text{B}|^{11}\text{B}|^{10}\text{B}$, $^{11}\text{B}|^{10}\text{B}|^{10}\text{B}$, and 4-slab heterostructure $^{11}\text{B}|^{10}\text{B}|^{11}\text{B}|^{10}\text{B}$ and $^{11}\text{B}|^{10}\text{B}|^{11}\text{B}|^{10}\text{B}$, show unique s-SNOM oscillations (Fig. 2) that all differ from each other.

Engineer polariton dispersions in isotopic heterostructures

vdW isotope heterostructuring of HPPs is unambiguously revealed in the ω - k dispersions of isotopic heterostructures that are unique at each composition and stacking (Fig. 3). The experimental data (red circles) by Fourier Transform of the s-SNOM images and profiles (Supplementary Note 1) agree excellently with the electromagnetics (EM) calculation of the complex reflectivity of the isotopic heterostructures (false color, Supplementary Note 2). HPPs can be engineered by varying the composition of the isotopic heterostructures: 1 ^{10}B slab + 1 ^{11}B slab (Fig. 3a, b), 1 ^{10}B slab + 2 ^{11}B slabs (Fig. 3c–e), 2 ^{10}B slab + 1 ^{11}B slabs (Fig. 3f–h), and 2 ^{10}B slab + 2 ^{11}B slabs (Fig. 3i, j), all reveal unique dispersions.

Note that current hyperbolic systems have been following the universal even ω - k dispersion³³ (Fig. 4): adjacent polariton branches are separated by identical momentum Δk (red arrows). This universal response originates from the Fabry-Perot quantization condition²¹:

$$\Delta\varphi = 2k_z d + \varphi_{R_sub} + \varphi_{R_sup} = 2\pi N. \quad (1)$$

$\Delta\varphi$ is the phase accumulation of HPPs, $k_z = \sqrt{\epsilon_t(\omega/c)^2 - k^2\epsilon_t/\epsilon_z}$ is the vertical momentum, d is the thickness of the hyperbolic slab, φ_{R_sub} and φ_{R_sup} are the phase of HPP reflection at the substrate and superstrate, and $N = 1, 0$, and -1 , etc., is an integer and varies at different dispersion branches (e.g., Figs. 3–4). At large k , $k_z \cong ik\sqrt{\epsilon_t/\epsilon_z}$ and $k = \frac{i}{d}\sqrt{\frac{\epsilon_z}{\epsilon_t}(-\pi N + \frac{\varphi_{R_sub} + \varphi_{R_sup}}{2})}$. Therefore, adjacent HPP branches are evenly separated by an identical momentum $\frac{i}{d}\sqrt{\frac{\epsilon_z}{\epsilon_t}}\pi$ —the universal even-dispersion. Although HPPs can be altered by state-of-the-art methods of substrate engineering^{45,46}, coupling with graphene⁴⁷ and phase change materials^{48–50}, HPP branches therein were altered to the same degree: they are shifted by an identical Δk and still follow the universal even-dispersion.

Remarkably, vdW isotope heterostructuring introduced here breaks this universal response by providing HPPs with a variety of dispersions. In $\omega = 1350$ – 1400 cm^{-1} , $^{10}\text{B}|^{10}\text{B}|^{11}\text{B}$ (Fig. 3f) shows only 1 polariton branch instead of the conventional unlimited numbers of branches in hyperbolic materials. $^{10}\text{B}|^{11}\text{B}|^{11}\text{B}$ (Fig. 3c) and $^{10}\text{B}|^{11}\text{B}|^{10}\text{B}|^{11}\text{B}$ (Fig. 3j) show 2 branches with stronger $N = 1$ branches. $^{11}\text{B}|^{10}\text{B}|^{11}\text{B}$ (Fig. 3d) exhibits approaching branches (see black arrows as a guide to the eye): the $N = 1$ and $N = 0$ branches are merging where the $N = 1$ branch fades at 1390 cm^{-1} while the $N = 0$ one extends to the higher ω . $^{10}\text{B}|^{11}\text{B}|^{10}\text{B}|^{11}\text{B}$ in Fig. 5e and other compositions in Supplementary Note 3 reveal merging branches: adjacent polariton branches merges. In addition, $^{11}\text{B}|^{10}\text{B}|^{11}\text{B}|^{10}\text{B}$ (Fig. 3i) supports unbalanced

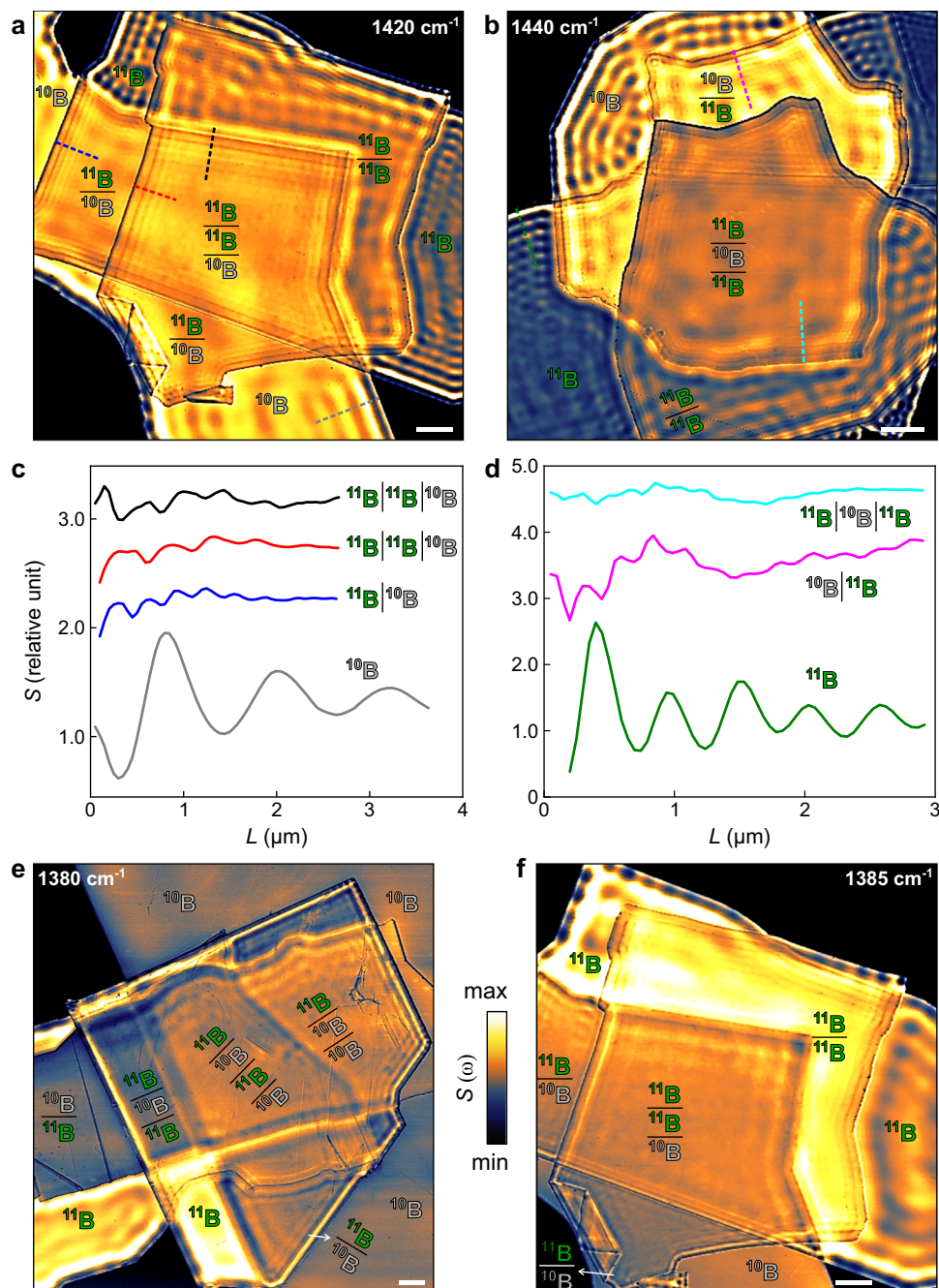


Fig. 2 | The scattering-type scanning near-field optical microscopy (s-SNOM) nano-infrared images of phonon polaritons in hBN isotopic heterostructures. s-SNOM amplitude images of ^{10}B - ^{11}B isotopic heterostructures at representative infrared (IR) frequency $\omega = 1440\text{ cm}^{-1}$ (a), 1420 cm^{-1} (b), 1380 cm^{-1} (e), and 1385 cm^{-1} (f). c, d s-SNOM profiles cut along dashed lines in (a) and (b) reveal short-period

beats in ^{10}B - ^{11}B isotopic heterostructures (black, red, blue, cyan, and pink) and long-period fringes in single slab ^{10}B and ^{11}B hBN (gray and green). L is the distance from the slab or heterostructure edge. Scale bar: $2\text{ }\mu\text{m}$. The compositions of ^{10}B and ^{11}B building blocks in each region are denoted by the stacking from top to bottom.

branches: the $N=0$ branch is significantly weaker than the other polariton branches.

The advanced capabilities of vdW isotope heterostructuring in engineering polariton ω - k dispersions originate from the fundamental virtue that atomic masses of the same element inside polaritonic systems can vary locally and be spatially engineered. Specifically, the atomic mass spatial-heterogeneity modifies the local permittivity, thus locally varying k_z in ^{10}B and ^{11}B subregions and introducing additional phase jumps of HPP transmission and reflection ($\varphi_{T,10/11}$ and $\varphi_{R,10/11}$) at ^{10}B - ^{11}B interfaces inside the isotopic heterostructures (see Supplementary Note 4 for the detailed analysis). Therefore, the original Fabry-

Perot quantization condition (Eq. 1) is modified. HPPs in ^{10}B - ^{11}B isotopic heterostructures can differ from those in isotope-homogenous systems and be engineered into a variety of ω - k dispersions that break the universal even-dispersion.

In addition to the composition, HPPs can be engineered by varying the stacking of ^{10}B and ^{11}B building blocks. For 2-slab heterostructures with the same composition of 1 ^{10}B slab + 1 ^{11}B slab (Fig. 3a, b), $^{11}\text{B}|^{10}\text{B}$ stacking (Fig. 3a) supports multiple HPP branches spanning from $\omega = 1360$ to 1400 cm^{-1} , whereas $^{10}\text{B}|^{11}\text{B}$ stacking (Fig. 3b) supports a single branch at $\omega = 1360$ to 1380 cm^{-1} . In 3-slab heterostructures with the composition of 1 ^{10}B slab + 2 ^{11}B slabs, three

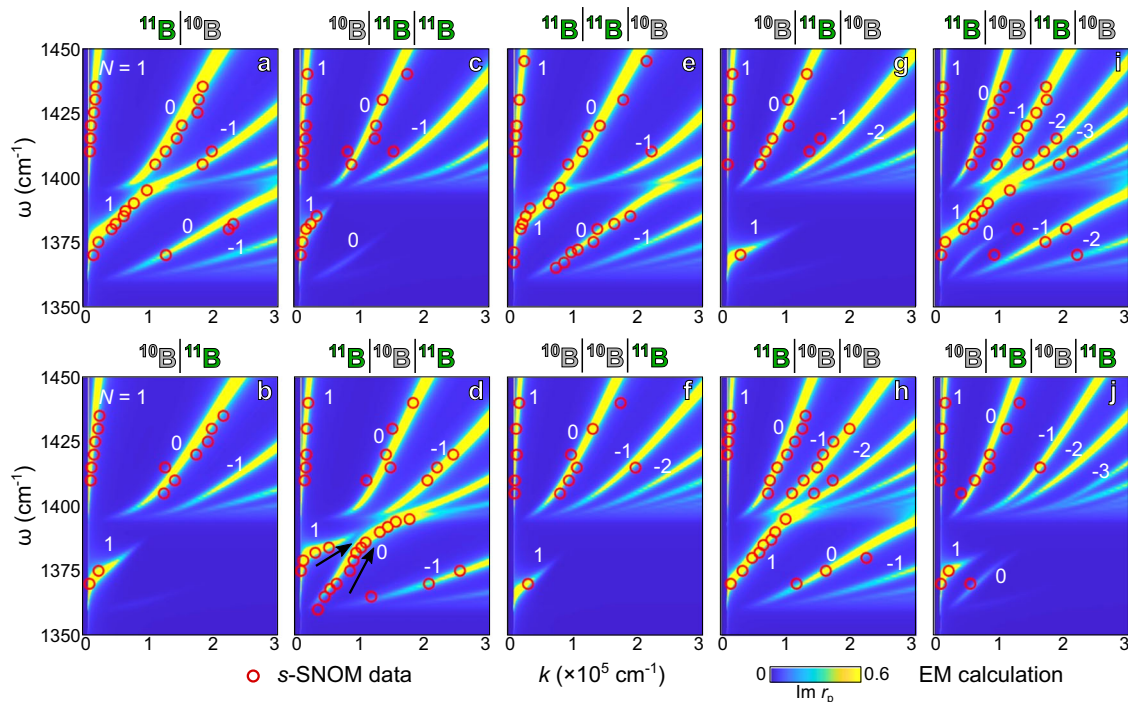


Fig. 3 | Energy-momentum (ω - k) dispersions reveal the tailoring of phonon polaritons in isotopic heterostructures by varying the compositions and stacking of the ^{10}B and ^{11}B building blocks. Engineered phonon polaritons in 2-slab (a, b), 3-slab (c–h), and 4-slab (i, j) isotopic heterostructures with the composition and stacking denoted from top to bottom (above the dispersion plots).

Various polariton branches are marked by $N=1, 0$, and -1 , etc. Black arrows in (d) indicate the two dispersion branches approach together. The s-SNOM experimental data and modeling results from the electromagnetics (EM) calculation of the reflectivity are plotted with red circles and false-color maps, respectively.

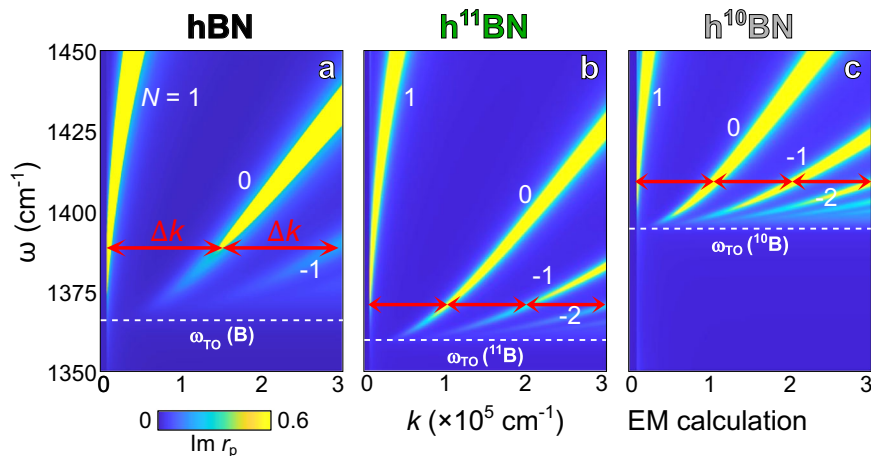


Fig. 4 | Universal even energy-momentum (ω - k) dispersions in isotope-homogeneous hyperbolic systems. a–c The ω - k dispersions of naturally abundant hBN, $h^{11}\text{BN}$, and $h^{10}\text{BN}$, respectively. Thickness: 50 nm. Adjacent polariton branches are separated evenly by identical momentum Δk (red arrows) in all panels. White

dashed lines indicate the transverse optical (TO) phonon frequencies of naturally abundant hBN, $h^{10}\text{BN}$, and $h^{11}\text{BN}$, respectively. Various polariton branches are marked by $N=1, 0$, and -1 , etc.

types of stackings possess all different dispersions: 2 branches for $^{10}\text{B}|^{11}\text{B}|^{11}\text{B}$ (Fig. 3c), approaching branches for $^{11}\text{B}|^{10}\text{B}|^{11}\text{B}$ (Fig. 3d), and evenly distributed branches for $^{11}\text{B}|^{11}\text{B}|^{10}\text{B}$ (Fig. 3e). This stacking engineering is also revealed in 3-slab heterostructures of 2 ^{10}B slabs + 1 ^{11}B slab (Fig. 3f–h) and 4-slab heterostructures of 2 ^{10}B slabs + 2 ^{11}B slabs (Fig. 3i, j): each stacking leads to unique HPP dispersion.

vdW isotope heterostructuring is not limited to varying the composition and stacking. The thickness of each building block is another degree of freedom to engineer the overall properties of the isotopic heterostructure. In Fig. 5a–c, we plot the combined

experimental and theoretical dispersions in 3-slab isotopic heterostructures with identical composition and stacking $^{11}\text{B}|^{10}\text{B}|^{11}\text{B}$ yet different thicknesses of the ^{10}B and ^{11}B building blocks. These dispersions show evident thickness dependence. The thickness of 27|23|35 nm (for $^{11}\text{B}|^{10}\text{B}|^{11}\text{B}$, Fig. 5a) exhibits approaching branches: the $N=1$ branch stops at $\omega \sim 1385 \text{ cm}^{-1}$, whereas the $N=0$ branch extends into $\omega > 1400 \text{ cm}^{-1}$. The thickness of 25|27|16 nm (Fig. 5b) exhibits unbalanced branches: the $N=1$ branch extends into $\omega > 1400 \text{ cm}^{-1}$, whereas the $N=0$ branch is relatively weak and stops at $\omega \sim 1380 \text{ cm}^{-1}$. Another thickness of 6|11|9 nm (Fig. 5c) shows

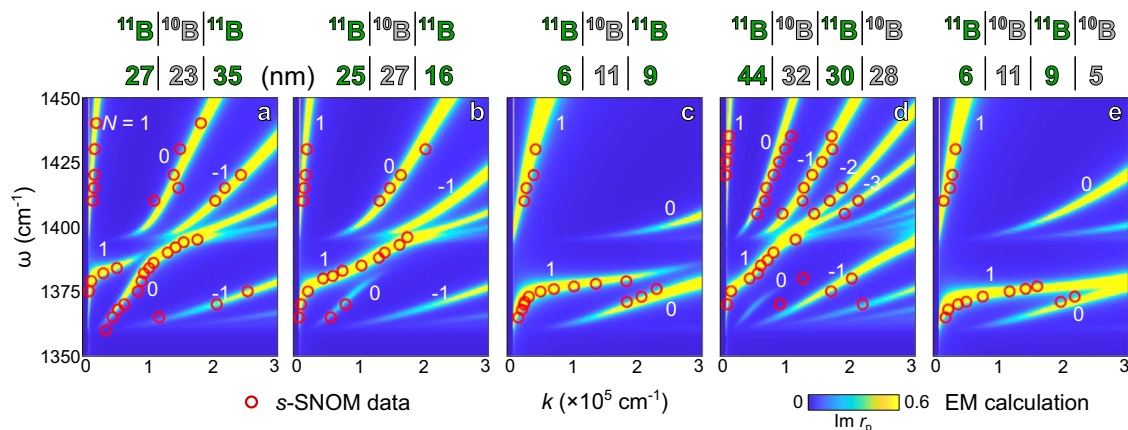


Fig. 5 | Energy-momentum (ω - k) dispersions reveal the tailoring of phonon polaritons in isotopic heterostructures by varying the thicknesses of the ^{10}B and ^{11}B building blocks. a–d Phonon polaritons in 3-slab isotopic heterostructures with the identical composition and stacking $^{11}\text{B}|^{10}\text{B}|^{11}\text{B}$ but with the thickness of 27|23|35 nm (a), 25|27|16 nm (b), and 6|11|9 nm (c). **d, e** Phonon polaritons in

4-slab isotopic heterostructures with the identical composition and stacking $^{11}\text{B}|^{10}\text{B}|^{11}\text{B}|^{10}\text{B}$ but with the thickness of 44|32|30|28 nm (d) and 6|11|9|5 nm (e). Various polariton branches are marked by $N = 1, 0$, and -1 , etc. The s-SNOM data and modeling results are plotted with red circles and false-color maps, respectively.

balanced and approaching branches, and all HPP branches locate at larger k . The degree of freedom of building blocks' thicknesses is further verified in 4-slab isotopic heterostructures $^{11}\text{B}|^{10}\text{B}|^{11}\text{B}|^{10}\text{B}$: the thickness of 44|32|30|28 nm (Fig. 5d) shows unbalanced branches, whereas the thickness of 6|11|9|5 nm (Fig. 5e) shows balanced and merging branches.

Discussion

Combined experiments and theory in Figs. 1–5 showcase the method of vdW isotope heterostructuring in engineering HPPs in ^{10}B - ^{11}B isotopic heterostructures. A variety of energy-momentum dispersions are engineered to break the universal even-dispersion for hyperbolic systems and those engineered by state-of-the-art methods^{45–49}. These unique HPP dispersions engineered in isotopic heterostructures can be attributed to the EM interactions of the ^{10}B and ^{11}B hBN building blocks. As a result, the standard hyperbolic modes in ^{10}B and ^{11}B building blocks repulse and form ω - k dispersions. Importantly, the delicate EM interactions and mode repulsion depend strongly on the composition, stacking, and thickness of the ^{10}B and ^{11}B building blocks, therefore offering the degrees of freedom to tailor HPPs in ^{10}B - ^{11}B isotopic heterostructures. In Supplementary Note 5, we provide a detailed analysis of various ω - k dispersions of HPPs in ^{10}B - ^{11}B isotopic heterostructures from the perspective of EM interactions.

The highly-confined HPPs may be delicately engineered to offer on-demand nano-light by programming the isotope building blocks in isotopic heterostructures. Therefore, the HPPs can possess unique and tailorable energy-momentum dispersions and photonic density of states. These merits offer unique approaches to control nanoscale light-matter wave propagation, light emission, quantum optics, and energy transfer, thus expanding the current nanophotonic and thermal functionalities⁵¹. Due to the universality and importance of isotopes, the method of vdW isotope heterostructuring established here can apply to a broad range of materials and engineer thermal, electronic, magnetic, quantum, and other properties where atomic mass or nuclear spin plays a role. Future works may be directed towards extending vdW isotope heterostructuring from hBN to other materials where a series of monoisotopic crystals^{4,7–10,15} have been produced. Yet, their isotopic heterostructures are promising but remain unexplored. It is also worth building few-atomic-layer isotopic heterostructures where isotopic moiré superlattices can be involved to configure related material properties, including moiré superconductivity⁵², ferroelectricity⁵³, ferromagnetism⁵⁴, excitons^{55–58}, and many others^{59–64}. In addition, it may be valuable to investigate the optical responses of

interfaces within isotopic heterostructures, particularly at frequencies where the permittivity of the constituent slabs changes sign. Furthermore, while this work mainly exploits spatially engineered atomic masses to showcase vdW isotope heterostructuring, the other fundamental virtue of this method—spatially engineered nuclear spins—is equally promising and can be explored in spintronics^{18,65–67}, chemical reactions^{3,68}, and quantum information and technologies^{16–20}.

Methods

Fabrication of isotopic heterostructures

^{10}B - ^{11}B isotopic heterostructures were assembled using the standard vdW dry transfer method⁵². First, thin slabs of h^{10}BN and h^{11}BN were mechanically exfoliated from bulk monoisotopic crystals grown at atmospheric pressure from an iron-chromium flux⁶⁹. Poly (bisphenol A carbonate) (PC)/polydimethylsiloxane (PDMS) were then used to pick up h^{10}BN and h^{11}BN thin slabs and stack them together into ^{10}B - ^{11}B isotopic heterostructures.

Infrared nano-imaging

The infrared nano-imaging of polaritons in isotopic heterostructures was performed using the scattering-type scanning near-field optical microscope (s-SNOM, www.neaspec.com). The s-SNOM is a tapping-mode atomic force microscope (AFM) illuminated by monochromatic mid-IR quantum cascade lasers (QCLs) with a frequency coverage of 900–2300 cm^{-1} . In the experiment, the AFM tip (radius ~ 10 nm, PtIr coating) taps at the frequency of ~ 280 kHz and the amplitude of ~ 70 nm. The s-SNOM nano-images were obtained by the pseudo-heterodyne interferometric detection: the scattered signal from the AFM tip was collected and demodulated at the third harmonics of the tapping frequency to obtain the genuine near-field response.

Data availability

The data that support the findings of this study are available from the corresponding author upon request.

Code availability

The codes that support the findings of this study are available from the corresponding author upon request.

References

- Harilal, S. S., Brumfield, B. E., LaHaye, N. L., Hartig, K. C. & Phillips, M. C. Optical spectroscopy of laser-produced plasmas for standoff isotopic analysis. *Appl. Phys. Rev.* **5**, 021301 (2018).

2. Bauche, J. & Champeau, R.J. in *Advances in Atomic and Molecular Physics*, Vol. 12 (eds Bates, D. R. & Bederson, B.) 39–86 (Academic Press, 1976).
3. Gómez-Gallego, M. & Sierra, M. A. Kinetic isotope effects in the study of organometallic reaction mechanisms. *Chem. Rev.* **111**, 4857–4963 (2011).
4. Rodríguez-Nieva, J. F., Saito, R., Costa, S. D. & Dresselhaus, M. S. Effect of ^{13}C isotope doping on the optical phonon modes in graphene: Localization and Raman spectroscopy. *Phys. Rev. B* **85**, 245406 (2012).
5. Vuong, T. Q. P. et al. Isotope engineering of van der Waals interactions in hexagonal boron nitride. *Nat. Mater.* **17**, 152–158 (2018).
6. Haller, E. E. Isotopically controlled semiconductors. *Solid State Commun.* **133**, 693–707 (2005).
7. Chen, S. et al. Thermal conductivity of isotopically modified graphene. *Nat. Mater.* **11**, 203–207 (2012).
8. Cai, Q. et al. Outstanding thermal conductivity of single atomic layer isotope-modified boron nitride. *Phys. Rev. Lett.* **125**, 085902 (2020).
9. Chen, K. et al. Ultrahigh thermal conductivity in isotope-enriched cubic boron nitride. *Science* **367**, 555 (2020).
10. Li, X. et al. Isotope-engineering the thermal conductivity of two-dimensional MoS₂. *ACS Nano* **13**, 2481–2489 (2019).
11. Manley, M. E. et al. Giant isotope effect on phonon dispersion and thermal conductivity in methylammonium lead iodide. *Sci. Adv.* **6**, eaaz1842 (2020).
12. Cardona, M. & Thewalt, M. L. W. Isotope effects on the optical spectra of semiconductors. *Rev. Mod. Phys.* **77**, 1173–1224 (2005).
13. Maxwell, E. Isotope effect in the superconductivity of mercury. *Phys. Rev.* **78**, 477–477 (1950).
14. Sonntag, J. et al. Excellent electronic transport in heterostructures of graphene and monoisotopic boron nitride grown at atmospheric pressure. *2D Mater.* **7**, 031009 (2020).
15. Wu, W., Morales-Acosta, M. D., Wang, Y. & Pettes, M. T. Isotope effect in bilayer WSe₂. *Nano Lett.* **19**, 1527–1533 (2019).
16. Kane, B. E. A silicon-based nuclear spin quantum computer. *Nature* **393**, 133–137 (1998).
17. Balasubramanian, G. et al. Ultralong spin coherence time in isotopically engineered diamond. *Nat. Mater.* **8**, 383–387 (2009).
18. Itoh, K. M. & Watanabe, H. Isotope engineering of silicon and diamond for quantum computing and sensing applications. *MRS Commun.* **4**, 143–157 (2014).
19. Saeedi, K. et al. Room-temperature quantum bit storage exceeding 39 min using ionized donors in silicon-28. *Science* **342**, 830 (2013).
20. Wu, Y., Tong, Q., Liu, G.-B., Yu, H. & Yao, W. Spin-valley qubit in nanostructures of monolayer semiconductors: optical control and hyperfine interaction. *Phys. Rev. B* **93**, 045313 (2016).
21. Dai, S. et al. Tunable phonon polaritons in atomically thin van der Waals crystals of boron nitride. *Science* **343**, 1125–1129 (2014).
22. Xu, X. G. et al. One-dimensional surface phonon polaritons in boron nitride nanotubes. *Nat. Commun.* **5**, 4782 (2014).
23. Shi, Z. et al. Amplitude- and phase-resolved nanospectral imaging of phonon polaritons in hexagonal boron nitride. *ACS Photonics* **2**, 790–796 (2015).
24. Yoxall, E. et al. Direct observation of ultraslow hyperbolic polariton propagation with negative phase velocity. *Nat. Photonics* **9**, 674 (2015).
25. Caldwell, J. D. et al. Sub-diffractive volume-confined polaritons in the natural hyperbolic material hexagonal boron nitride. *Nat. Commun.* **5**, 5221 (2014).
26. Hu, G., Shen, J., Qiu, C.-W., Alù, A. & Dai, S. Phonon polaritons and hyperbolic response in van der Waals materials. *Adv. Opt. Mater.* **8**, 1901393 (2020).
27. Chen, M. et al. Configurable phonon polaritons in twisted $\alpha\text{-MoO}_3$. *Nat. Mater.* **19**, 1307–1311 (2020).
28. Dai, S. & Ma, Q. A twist for nanolight. *Nat. Mater.* **22**, 805–806 (2023).
29. Chen, M. et al. Altering the reflection phase for nano-polaritons: a case study of hyperbolic surface polaritons in hexagonal boron nitride. *Adv. Opt. Mater.* **10**, 2102723 (2022).
30. Shen, J. et al. Hyperbolic phonon polaritons with positive and negative phase velocities in suspended $\alpha\text{-MoO}_3$. *Appl. Phys. Lett.* **120**, 113101 (2022).
31. Jacob, Z., Alekseyev, L. V. & Narimanov, E. Optical hyperlens: far-field imaging beyond the diffraction limit. *Opt. Express* **14**, 8247–8256 (2006).
32. Salandrino, A. & Engheta, N. Far-field subdiffraction optical microscopy using metamaterial crystals: theory and simulations. *Phys. Rev. B* **74**, 075103 (2006).
33. Poddubny, A., Iorsh, I., Belov, P. & Kivshar, Y. Hyperbolic metamaterials. *Nat. Photonics* **7**, 948 (2013).
34. Liu, Z., Lee, H., Xiong, Y., Sun, C. & Zhang, X. Far-field optical hyperlens magnifying sub-diffraction-limited objects. *Science* **315**, 1686–1686 (2007).
35. Yao, J. et al. Optical negative refraction in bulk metamaterials of nanowires. *Science* **321**, 930–930 (2008).
36. Liu, Y. & Zhang, X. Metasurfaces for manipulating surface plasmons. *Appl. Phys. Lett.* **103**, 141101 (2013).
37. Gomez-Diaz, J. S., Tymchenko, M. & Alù, A. Hyperbolic plasmons and topological transitions over uniaxial metasurfaces. *Phys. Rev. Lett.* **114**, 233901 (2015).
38. High, A. A. et al. Visible-frequency hyperbolic metasurface. *Nature* **522**, 192 (2015).
39. Kumar, A., Low, T., Fung, K. H., Avouris, P. & Fang, N. X. Tunable light-matter interaction and the role of hyperbolicity in graphene-hBN system. *Nano Lett.* **15**, 3172–3180 (2015).
40. Wei, D., Harris, C. & Law, S. Volume plasmon polaritons in semiconductor hyperbolic metamaterials. *Opt. Mater. Express* **7**, 2672–2681 (2017).
41. Atkin, J. M., Berweger, S., Jones, A. C. & Raschke, M. B. Nano-optical imaging and spectroscopy of order, phases, and domains in complex solids. *Adv. Phys.* **61**, 745–842 (2012).
42. Low, T. et al. Polaritons in layered two-dimensional materials. *Nat. Mater.* **16**, 182 (2016).
43. Basov, D. N., Fogler, M. M. & García de Abajo, F. J. Polaritons in van der Waals materials. *Science* **354**, aag1992 (2016).
44. Giles, A. J. et al. Ultralow-loss polaritons in isotopically pure boron nitride. *Nat. Mater.* **17**, 134 (2017).
45. Dai, S. et al. Hyperbolic phonon polaritons in suspended hexagonal boron nitride. *Nano Lett.* **19**, 1009–1014 (2019).
46. Fali, A. et al. Refractive index-based control of hyperbolic phonon-polariton propagation. *Nano Lett.* **19**, 7725–7734 (2019).
47. Dai, S. et al. Graphene on hexagonal boron nitride as a tunable hyperbolic metamaterial. *Nat. Nanotechnol.* **10**, 682 (2015).
48. Folland, T. G. et al. Reconfigurable infrared hyperbolic metasurfaces using phase change materials. *Nat. Commun.* **9**, 4371 (2018).
49. Dai, S. et al. Phase-Change Hyperbolic Heterostructures for Nanopolaritons: A Case Study of hBN/VO₂. *Adv. Mater.* **31**, 1900251 (2019).
50. Chaudhary, K. et al. Polariton nanophotonics using phase-change materials. *Nat. Commun.* **10**, 4487 (2019).
51. Cunha, J. et al. Controlling light, heat, and vibrations in plasmonics and phononics. *Adv. Opt. Mater.* **8**, 2001225 (2020).
52. Cao, Y. et al. Unconventional superconductivity in magic-angle graphene superlattices. *Nature* **556**, 43 (2018).
53. Yasuda, K., Wang, X., Watanabe, K., Taniguchi, T. & Jarillo-Herrero, P. Stacking-engineered ferroelectricity in bilayer boron nitride. *Science* **372**, 1458 (2021).

54. Sharpe, A. L. et al. Emergent ferromagnetism near three-quarters filling in twisted bilayer graphene. *Science* **365**, 605–608 (2019).
55. Tran, K. et al. Evidence for moiré excitons in van der Waals heterostructures. *Nature* **567**, 71–75 (2019).
56. Alexeev, E. M. et al. Resonantly hybridized excitons in moiré superlattices in van der Waals heterostructures. *Nature* **567**, 81–86 (2019).
57. Jin, C. et al. Observation of moiré excitons in WSe₂/WS₂ heterostructure superlattices. *Nature* **567**, 76–80 (2019).
58. Seyler, K. L. et al. Signatures of moiré-trapped valley excitons in MoSe₂/WSe₂ heterobilayers. *Nature* **567**, 66–70 (2019).
59. Krishna Kumar, R. et al. High-temperature quantum oscillations caused by recurring Bloch states in graphene superlattices. *Science* **357**, 181–184 (2017).
60. Lee, M. et al. Ballistic miniband conduction in a graphene superlattice. *Science* **353**, 1526–1529 (2016).
61. Spanton, E. M. et al. Observation of fractional Chern insulators in a van der Waals heterostructure. *Science* **360**, 62–66 (2018).
62. Hunt, B. et al. Massive Dirac fermions and Hofstadter butterfly in a van der Waals heterostructure. *Science* **340**, 1427–1430 (2013).
63. Alden, J. S. et al. Strain solitons and topological defects in bilayer graphene. *Proc. Natl Acad. Sci.* **110**, 11256 (2013).
64. Yankowitz, M. et al. Tuning superconductivity in twisted bilayer graphene. *Science* **363**, 1059 (2019).
65. Tayler, M. C. D. & Levitt, M. H. Accessing long-lived nuclear spin order by isotope-induced symmetry breaking. *J. Am. Chem. Soc.* **135**, 2120–2123 (2013).
66. Bourassa, A. et al. Entanglement and control of single nuclear spins in isotopically engineered silicon carbide. *Nat. Mater.* **19**, 1319–1325 (2020).
67. Shlimak, I. Isotopically engineered Si and Ge for spintronics and quantum computation. *J. Magn. Magn. Mater.* **321**, 884–887 (2009).
68. Buchachenko, A. L. Magnetic isotope effect: nuclear spin control of chemical reactions. *J. Phys. Chem. A* **105**, 9995–10011 (2001).
69. Li, J. et al. Single crystal growth of monoisotopic hexagonal boron nitride from a Fe–Cr flux. *J. Mater. Chem. C* **8**, 9931–9935 (2020).

Acknowledgements

Work at Auburn University was supported by the National Science Foundation under Grant No. DMR-2238691, DMR-2005194, and ACS PRF fund 66229-DNI6. Support for hBN crystal growth was provided by the Office of Naval Research, award number N00014-20-1-2474. Q.M. and P.-J.H. acknowledge the support from AFOSR grant FA9550-21-1-0319.

Author contributions

S.D. and M.C. conceived the idea and designed the experiments. M.C. performed the optical experiments. M.C., E.H., and Z.Z. prepared the samples. J.L. and J.E. provided the monoisotopic crystals. Y.Z., J.-S.W., X.L., and H.C. developed the theory. M.C. and S.D. analyzed the data. M.C. and S.D. wrote the manuscript with input and comments from all authors. S.D., X.L., P.J.-H., Q.M., and J.E. supervised the project.

Competing interests

The authors declare no competing interests.

Additional information

Supplementary information The online version contains supplementary material available at <https://doi.org/10.1038/s41467-023-40449-w>.

Correspondence and requests for materials should be addressed to S. Dai.

Peer review information *Nature Communications* thanks the anonymous reviewer(s) for their contribution to the peer review of this work. A peer review file is available.

Reprints and permissions information is available at <http://www.nature.com/reprints>

Publisher's note Springer Nature remains neutral with regard to jurisdictional claims in published maps and institutional affiliations.

Open Access This article is licensed under a Creative Commons Attribution 4.0 International License, which permits use, sharing, adaptation, distribution and reproduction in any medium or format, as long as you give appropriate credit to the original author(s) and the source, provide a link to the Creative Commons licence, and indicate if changes were made. The images or other third party material in this article are included in the article's Creative Commons licence, unless indicated otherwise in a credit line to the material. If material is not included in the article's Creative Commons licence and your intended use is not permitted by statutory regulation or exceeds the permitted use, you will need to obtain permission directly from the copyright holder. To view a copy of this licence, visit <http://creativecommons.org/licenses/by/4.0/>.

© The Author(s) 2023